A Dual-Side Controlled Inductive Power Transfer System Optimized for Large Coupling Factor Variations and Partial Load

Tobias Diekhans and Rik W. De Doncker, *Fellow, IEEE*

***Abstract*—In this study, a 3-kW inductive power transfer system is investigated, specifically intended for contactless vehicle charging. A series-series-compensated topology with dual-side power control and a corresponding control strategy is proposed to significantly increase the overall efficiency, especially for systems with large coupling factor variations and in partial load mode. The topology, which is closely related to the dual-active bridge converter, enables the dual-side power control without adding additional dc/dc converters to the system, and thus keeping the additional hardware effort minimal. A detailed analysis of the proposed topology is provided, and the benefits of the dual-side control are demonstrated both theoretically and experimentally. A hardware prototype is built and a peak dc-to-dc efficiency of 95.8% at 100 mm air gap and a minimal efficiency of 92.1% at 170 mm air gap is measured, including the power electronic components. The partial load efficiency at 500 W output power is still as high as 90.6% at 135 mm air gap. Overall, the proposed topology provides a practical method to overcome the main drawback of most single-side controlled inductive power transfer systems, which is a significant efficiency drop outside the nominal operating point.**

***Index Terms*—Contactless power transfer (CPT), inductive power transfer (IPT), wireless charging, wireless power transfer (WPT).**

I. Introduction

SYSTEMS for contactless inductive power transfer (IPT) are well known in many applications, such as industrial automation, medical implants, clean rooms, and consumer electronics [1], [2]. The technology has the potential to significantly facilitate the charging process of electric vehicles in comparison to conventional conductive chargers as it eliminates the need for the driver to manually handle a charging cable. The main challenges in applying IPT to contactless vehicle charging are the large air gap due to the ground clearance of the vehicle and the variable vehicle position above the charging pad. At the same time, a contactless vehicle charger must be safe, robust, efficient, and apt to be manufactured at low costs, to compete with conventional conductive chargers.

Manuscript received September 30, 2014; revised November 24, 2014; accepted January 4, 2014. Date of publication January 19, 2015; date of current version July 10, 2015. Recommended for publication by Associate Editor J. Boys.

T. Diekhans is with the Robert Bosch GmbH, Central Research, 70049 Stuttgart, Germany (e-mail: tobias.diekhans@de.bosch.com).

R. W. De Doncker is with the Institute for Power Electronics and Electrical Drives, RWTH Aachen University, 52066 Aachen, Germany (e-mail: post@isea.rwth-aachen.de).

Color versions of one or more of the figures in this paper are available online at http://ieeexplore.ieee.org.

Digital Object Identifier 10.1109/TPEL.2015.2393912

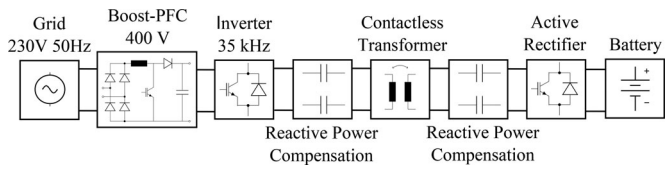

Fig. 1. Schematic of the contactless vehicle charger.

The primary coil on the infrastructure side and the secondary coil on the vehicle side are magnetically coupled and can be described as a loosely coupled transformer. Due to the large leakage inductances, reactive power compensation is required both on the primary and the secondary side. The most common topology uses an *LCL* resonant tank on the primary side and a parallel-tuned pickup coil where power control can be applied on the primary side [3], [4], the secondary side [5]–[7], or on both sides [8].

Another popular topology for IPT is the series-compensated primary and secondary coil [9]–[15]. Its current source behavior on the secondary side when operated with a voltage source inverter on the primary side also makes it a good candidate for battery-charging applications. Power control is typically performed on the primary side either by using a phase-shifted full-bridge or by regulating the input dc-link voltage, allowing the full-bridge to operate under soft-switching conditions. In a separate publication, a detailed simulative topology comparison between different series-series-compensated hard- and soft-switching topologies was performed [16].

Current research activities tend to increase the operating frequency and to apply soft-switching topologies. However, in this study, it is shown that high efficiencies can also be achieved with a hard-switching topology if a dual-side power control is applied. The main benefit is a wide operating range regarding coupling factor and battery voltage variation, as well as partial load. Furthermore, the proposed topology is simple and robust and does not require additional dc/dc converters on the infrastructure or vehicle side for power control.

II. Proposed Topology

In this study, a 3-kW contactless vehicle charger is investigated that is operated from the 230-V single-phase grid. A schematic of the required power electronic components is shown in Fig. 1. First, the ac grid voltage is rectified using a power factor correction (PFC) rectifier. The PFC rectifier is not investigated in detail in this study because it is a standard component and can be designed mostly independently from the other components of

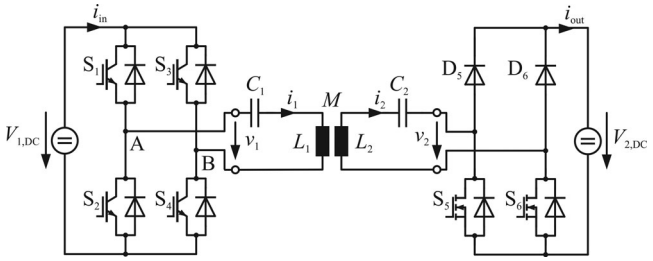

Fig. 2. Proposed dual-side controlled topology with series-series reactive power compensation.

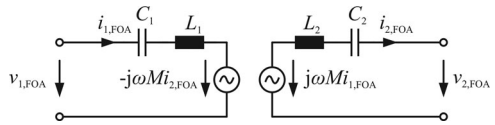

Fig. 3. Transformer equivalent circuit including reactive power compensation.

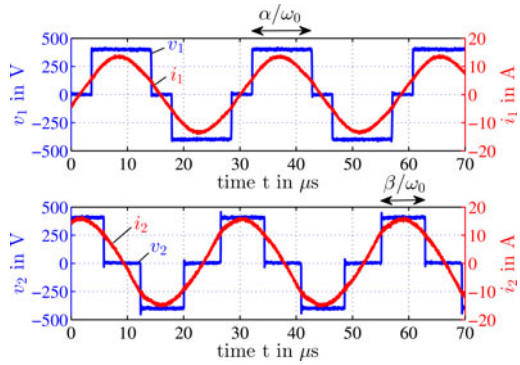

Fig. 4. Measured voltage and current waveforms using the proposed modulation scheme (135 mm air gap, 3 kW output power, $V_{1,\mathrm{DC}} = V_{2,\mathrm{DC}} = 400$ V).

the IPT system. The nominal efficiency of the PFC rectifier can be assumed to be in the range of 97% to 98%, or even higher for more complex topologies [17], [18]. Its output voltage is set to 400 V, which enables the use of standard 600-V semiconductor devices both in the PFC rectifier and the inverter. At the same time, the voltage is chosen above the ac input voltage amplitude to apply the conventional boost PFC topology.

In Fig. 2, the proposed dual-side controlled topology is depicted, involving inverter, reactive power compensation, contactless transformer, and rectifier. Series resonant capacitors, which match the coil inductances L_1 and L_2 at the operating frequency ω_0 according to (1), are applied both on the primary and secondary side. In practice, it is advantageous to split up the resonant capacitors and to build a symmetric resonant tank to reduce electromagnetic interference. For reasons of simplicity, this is not shown here

$$\omega_0 = \frac{1}{\sqrt{L_1 C_1}} = \frac{1}{\sqrt{L_2 C_2}}. \tag{1}$$

To describe the basic behavior of a series-series-compensated IPT system, first-order analysis (FOA) is performed first, and all higher harmonics and losses are neglected [19]. For this qualitative investigation, it is assumed that the impedances of the resonant capacitors C_1 and C_2 perfectly match the impedances of the coil inductances L_1 and L_2, respectively, at the resonant frequency ω_0. A fixed-frequency control is applied where the operating frequency equals the resonant frequency. The two basic voltage equations (2) and (3) can then be derived from the transformer equivalent circuit in Fig. 3, where M is the mutual inductance of the contactless transformer. The current directions were chosen according to the unidirectional power flow from the primary to the secondary side

$$v_{1,\mathrm{FOA}} = -\mathrm{j}\omega M i_{2,\mathrm{FOA}} \tag{2}$$

$$v_{2,\mathrm{FOA}} = \mathrm{j}\omega M i_{1,\mathrm{FOA}}. \tag{3}$$

The inverter is operated using the phase shift modulation scheme, where α is the phase shift between the two inverter legs. In Fig. 4, the resulting measured output voltage of the inverter v_1 is shown. The fundamental inverter output voltage $v_{1,\mathrm{FOA}}$ in dependence on the phase shift α can be calculated according to (4) by means of the Fourier transform

$$v_{1,\mathrm{FOA}} = \frac{2\sqrt{2}}{\pi} V_{1,\mathrm{DC}} \sin\left(\frac{\alpha}{2}\right). \tag{4}$$

With the primary voltage and current as shown in Fig. 4, the IGBTs of the leading inverter half-bridge are switched under zero current switching conditions with only turn-on switching losses. In contrast, the IGBTs of the lagging inverter half-bridge are operated under zero voltage switching conditions with only turn-off switching losses [12].

By introducing the two switches S_5 and S_6 into the rectifier, the power flow to the output can be controlled by the secondary side as well. In the free-wheeling state where both switches are closed, the current i_2 circulates on the secondary side, and in the state where both switches are opened, the current flows to the output capacitor. Both switches are switched in a way that there is zero phase shift between the resulting fundamental secondary voltage $v_{2,\mathrm{FOA}}$ and the fundamental secondary current $i_{2,\mathrm{FOA}}$ as shown in Fig. 4.

The pulse width β of the secondary voltage v_2 corresponds to the off-times of S_5 and S_6 and can be adjusted to reduce the fundamental output voltage $v_{2,\mathrm{FOA}}$. The functionality of the active rectifier is hence comparable to a passive rectifier followed by a boost converter. By means of the Fourier transform, the fundamental voltage $v_{2,\mathrm{FOA}}$ in dependence on the pulse width β can be calculated according to (5)

$$v_{2,\mathrm{FOA}} = \mathrm{j}\frac{2\sqrt{2}}{\pi} V_{2,\mathrm{DC}} \sin\left(\frac{\beta}{2}\right). \tag{5}$$

From the basic voltage equations of the transformer equivalent circuit (2) and (3), the corresponding fundamental currents in the primary and secondary winding of the contactless transformer can be derived

$$i_{1,\mathrm{FOA}} = \frac{2\sqrt{2}}{\pi}\frac{V_{2,\mathrm{DC}}}{\omega M} \sin\left(\frac{\beta}{2}\right) \tag{6}$$

$$i_{2,\mathrm{FOA}} = \mathrm{j}\frac{2\sqrt{2}}{\pi}\frac{V_{1,\mathrm{DC}}}{\omega M} \sin\left(\frac{\alpha}{2}\right). \tag{7}$$

TABLE I
QUALITATIVE INVESTIGATION OF THREE EXEMPLARY OPERATING POINTS

	Passive Rectifier ($\beta = \pi$)	Dual-Side Control according to (10)
Red. coupling: $M = \frac{1}{2} M_{\mathrm{N}}$	$i_{1,\mathrm{FOA}} = 2\, i_{1,\mathrm{FOA,N}}$ $i_{2,\mathrm{FOA}} = i_{2,\mathrm{FOA,N}}$	$i_{1,\mathrm{FOA}} = \sqrt{2}\, i_{1,\mathrm{FOA,N}}$ $i_{2,\mathrm{FOA}} = \sqrt{2}\, i_{2,\mathrm{FOA,N}}$
Partial load: $P = \frac{1}{4} P_{\mathrm{N}}$	$i_{1,\mathrm{FOA}} = i_{1,\mathrm{FOA,N}}$ $i_{2,\mathrm{FOA}} = \frac{1}{4}\, i_{2,\mathrm{FOA,N}}$	$i_{1,\mathrm{FOA}} = \frac{1}{2}\, i_{1,\mathrm{FOA,N}}$ $i_{2,\mathrm{FOA}} = \frac{1}{2}\, i_{2,\mathrm{FOA,N}}$
Variable battery voltage $V_{2,\mathrm{DC}}$	$i_{1,\mathrm{FOA}} \neq i_{1,\mathrm{FOA,N}}$ $i_{2,\mathrm{FOA}} \neq i_{1,\mathrm{FOA,N}}$	$i_{1,\mathrm{FOA}} = i_{1,\mathrm{FOA,N}}$ $i_{2,\mathrm{FOA}} = i_{2,\mathrm{FOA,N}}$

It can be noted that the secondary coil current can be directly controlled by the primary inverter pulse width α. Due to the current source behavior of the series-series reactive power compensation, this current is independent of the output voltage $V_{2,\mathrm{DC}}$ or the rectifier pulse width β. In the same way, the primary coil current can be controlled by the secondary rectifier pulse width β. The possibility to control the primary current using a fixed-frequency control would be lost if a passive rectifier was used.

Due to the bandpass characteristic of the series resonant tanks, the primary and secondary currents are approximately sinusoidal and higher harmonics do not significantly contribute to the power flow. Thus, the power transfer from the primary to the secondary side, if all losses are neglected, can be calculated from (5) and (7)

$$P_{\mathrm{out,FOA}} = \Re\left\{v_{2,\mathrm{FOA}}\, i^{*}_{2,\mathrm{FOA}}\right\} = \frac{8}{\pi^2}\frac{V_{1,\mathrm{DC}} V_{2,\mathrm{DC}}}{\omega M}\sin\left(\frac{\alpha}{2}\right)\sin\left(\frac{\beta}{2}\right). \tag{8}$$

III. PROPOSED CONTROL STRATEGY

According to (8), both control variables, the primary pulse width α and the secondary pulse width β, can control the power flow. This additional degree of freedom introduced by the dual-side control can be used to adjust the operating point, to optimally distribute the losses between the primary and secondary charging pads and to maximize the overall efficiency.

The proposal for an optimal control strategy is to keep the ratio between the fundamental primary current $i_{1,\mathrm{FOA}}$ and the secondary current $i_{2,\mathrm{FOA}}$ constant at all operating points to achieve an impedance match of the secondary load. The proposed optimal ratio depends on the nominal dc-link voltage $V_{1,\mathrm{DC,N}}$ and the nominal battery voltage $V_{2,\mathrm{DC,N}}$, for which the contactless transformer is designed according to (10). From (6) and (7), the resulting condition for the pulse widths α and β can be derived

$$\frac{|i_{1,\mathrm{FOA}}|}{|i_{2,\mathrm{FOA}}|} \stackrel{!}{=} \frac{V_{2,\mathrm{DC,N}}}{V_{1,\mathrm{DC,N}}} \tag{9}$$

$$\Rightarrow \frac{V_{1,\mathrm{DC}}}{V_{1,\mathrm{DC,N}}}\sin\left(\frac{\alpha}{2}\right) = \frac{V_{2,\mathrm{DC}}}{V_{2,\mathrm{DC,N}}}\sin\left(\frac{\beta}{2}\right). \tag{10}$$

The motivation for choosing this control strategy is explained qualitatively on the basis of three exemplary operating points that are of special interest in practice (see Table I). In the first case, it is discussed how the IPT system behaves if the mutual inductance M between the primary and secondary charging coils is reduced by a factor of 2, e.g., because of an inexact positioning of the vehicle. If the rectifier is purely passive, the primary current would double to achieve the same power transfer, causing significantly increased losses on the primary side. With the proposed dual-side control, both the primary and the secondary current are increased, but only by a factor of $\sqrt{2}$, causing lower overall losses on the system level.

In the second case, it is discussed how the IPT system behaves in partial load mode with a reduction of the output power to 25% of the nominal power. Using only a passive rectifier, a constantly high primary current would be circulating according to (6), because the IPT system is loaded with a constant voltage load (battery) rather than an ohmic load. Hence, the primary losses cannot be decreased, causing a significantly reduced partial load efficiency. With the proposed dual-side control, in contrast, both the primary and secondary currents can be reduced by a factor of 2 (see Table I) and a much higher partial load efficiency can be expected. This effect is demonstrated later experimentally.

Another benefit of the dual-side control is the decoupling of the IPT system's operating point from the actual battery voltage (third case in Table I) due to the boost functionality of the active rectifier. In practice, the battery voltage varies depending on its state of charge, the temperature, and other parameters. However, with the dual-side control, the IPT system can still be kept in its nominal operating point.

A possible control loop to realize the proposed dual-side control strategy is shown in Fig. 5. The inner control loop can be implemented on the secondary side without the need for wireless communication between the primary and secondary controller. Depending on the charging state of the battery, the inner control loop can either control the battery current (CC-mode) or battery voltage (CV-mode).

The outer control loop can be implemented on the primary side to adjust the operating point of the IPT system according to (9). Two signals have to be transmitted via a wireless communication channel from the secondary controller to the primary controller: The measured battery voltage $V_{2,\mathrm{DC,meas}}$ and the desired secondary pulse width β_{ref}. The outer control loop must be implemented much slower than the inner control loop to take into account the delay of the wireless communication channel. Measurements of the ac currents in the transformer windings are not needed for the control. However, these current measurements might be necessary to detect possible overcurrents.

IV. SIMULATION MODELS

In the design process, the main goal was to build an IPT system that is tolerant toward a certain variation of the magnetic coupling factor between the primary and the secondary coil. In the application as a contactless vehicle charger, this allows for a higher tolerance against variable air gaps of different vehicles or a misplacement of the vehicle above the charging pad. To account for this design goal, the IPT system has not only been

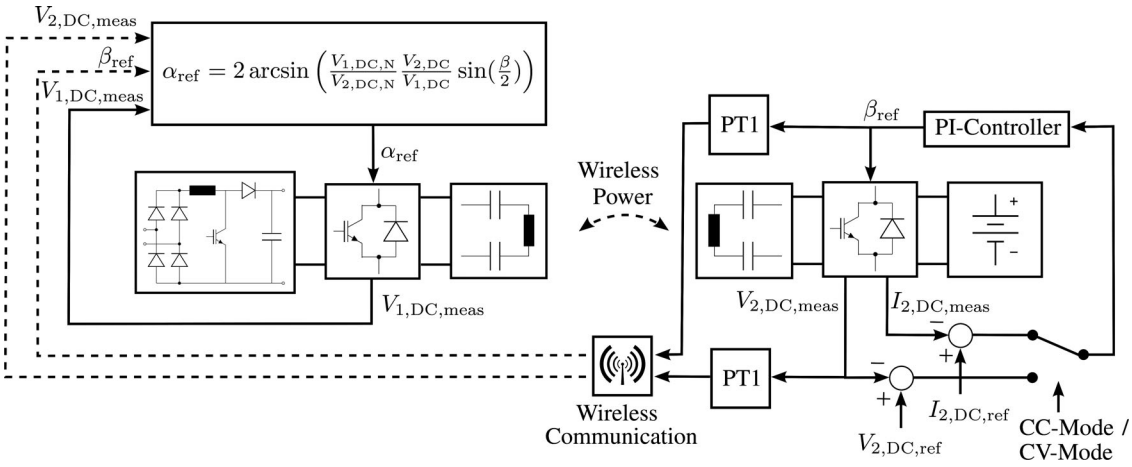

Fig. 5. Schematic of the control loop.

optimized for one single air gap and operating point but also for an air gap variation from 100 to 170 mm.

On the one hand, the aim was to achieve a high overall efficiency. On the other hand, the material effort regarding the copper and ferrite mass and the semiconductor chip size should be close to that of a practical implementation. To achieve an optimal system design, a holistic approach is necessary, involving the contactless transformer itself and also the power electronic components. For this purpose, all components were thoroughly modeled, and the total system was optimized using a multiobjective optimization approach. In this section, a brief overview of the implemented simulation models is given.

The distribution of the magnetic flux density in the air gap of the contactless transformer is simulated using the finite-element method (FEM). From the magnetic flux density distribution, the self-inductances L_1 and L_2 and the mutual inductance M at different air gaps are obtained. Furthermore, the stray magnetic field next to the vehicle is simulated.

The windings of the contactless transformer are built of high-frequency litz wire to reduce the impact of skin and proximity effect. In the simulation model, the skin effect (in the single strands of the litz wire) and the inner proximity effect (between the single strands of the litz wire) are calculated analytically with an empirical correction to account for the imperfect stranding of practically fabricated litz wires [20], [21]. The influence of the outer proximity effect due to external H-fields, e.g., caused by neighboring windings, is simulated using the 2-D-FEM tool FEMM.

The core losses of the contactless transformer are modeled based on the empirical Steinmetz equation [16], [22]. The Steinmetz equation can be applied because the excitation of the ferrite core is nearly sinusoidal without premagnetization of the core material. The inhomogeneous flux distribution inside the ferrite core is obtained from FEM simulations and considered in the loss calculation. The influence of the core geometry on the eddy current losses is neglected [23].

Above the secondary ferrite core, an aluminum shielding plate is installed to avoid eddy currents in the car underfloor. The eddy current losses in the aluminum shield are modeled based on the assumption that the thickness of the shield is much higher than the skin depth of the induced eddy currents (inductance-limited case) [16], [24]. The conductivity of the aluminum alloy $\mathrm{AlMg_3}$ which is used as shielding plate is assumed to $\sigma = 23$ MS/m.

The power electronic circuit is simulated using the commercial tool PLECS. The conduction losses of the chosen semiconductors are extracted from the corresponding datasheets. In addition, the switching losses were measured in a double-pulse test setup at different voltages, currents, and junction temperatures. From the double-pulse measurements, multidimensional look-up tables with the corresponding switching energies are obtained, which are embedded into the circuit simulator. The heat sink temperature of the thermal model is set to $T_{\mathrm{h}} = 100\,^{\circ}\mathrm{C}$.

Using these simulation models, the transformer geometry and power electronic components were designed and optimized. In the multiobjective optimization process, all important design parameters were variable: The size and geometry of the ferrite core, the number of primary and secondary turns, the stranding and the copper cross section of the litz wire. Regarding the power electronic components, the chip sizes of all IGBTs, MOSFETs and diodes were varied. On a system level, the most important design parameter was the operating frequency of the IPT system, as it affects both the design of the contactless transformer and the power electronic components.

V. Hardware Prototype

For experimental validation, a hardware prototype of the optimized IPT system that can transfer a nominal power of 3 kW over an air gap ranging from 100 to 170 mm was built. From the multiobjective optimization process, an operating frequency of 35 kHz was found to be optimal as it offers the best trade-off between the losses in the contactless transformer and the switching losses of the power electronics.

For the contactless transformer, a planar circular coil and a ferrite bar structure with an outer diameter of 600 mm and a thickness of 5 mm is chosen. A total ferrite mass of 4.8 kg and a total copper mass of 2.2 kg is used. The basic geometry data of the contactless transformer are given in Table II, and a

TABLE II
SPECIFICATIONS OF THE CONTACTLESS TRANSFORMER

Operating frequency:	35 kHz
Primary outer diameter:	600 mm
Primary ferrite mass:	2.4 kg
Primary copper mass:	1.4 kg
Secondary outer diameter:	600 mm
Secondary ferrite mass:	2.4 kg
Secondary copper mass:	0.8 kg

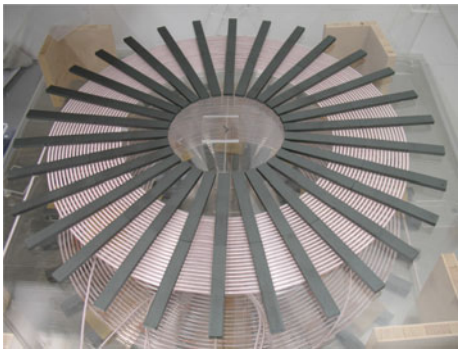

Fig. 6. Photograph of the secondary coil with alu shielding removed.

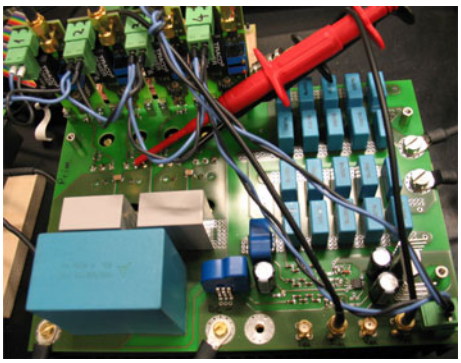

Fig. 7. Photograph of the inverter prototype.

photograph of the secondary coil with removed shielding plate is shown in Fig. 6.

The contactless transformer is built with $N_1 = 24$ turns on the primary side and $N_2 = 21$ turns on the secondary side. The primary litz wire consists of 630 strands, the secondary litz wire consists of 420 strands, both with a strand diameter of 0.1 mm (AWG 38). The ferrite core structure shown in Fig. 6 offers a good tradeoff between deployed ferrite material and achievable coupling factor and efficiency. Naturally, a better performance could be achieved with a closed ferrite plate. However, this would require significant overdimensioning as the ferrite thickness cannot be made arbitrarily small due to mechanical restrictions. The peak magnetic flux density in the ferrite bars is below 200 mT in all operating points, and hence, the ferrite is far from being saturated.

A photograph of the inverter prototype is shown in Fig. 7. For the primary full-bridge, high-speed IGBTs (Infineon IGW50N60H3) in combination with SiC-Schottky freewheeling diodes (Rohm SCS110AG) are chosen. The chosen IGBT is designed for low turn-off losses while the turn-on losses are additionally reduced by the improved reverse-recovery behavior of the SiC diodes.

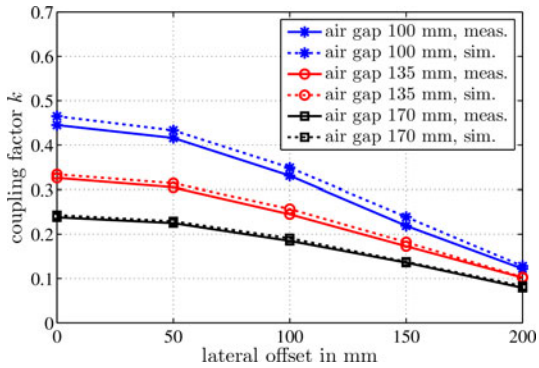

Fig. 8. Measured and simulated coupling factor at different coil positions.

For the active rectifier, superjunction MOSFETs (Infineon IPW60R099CP) in combination with SiC-Schottky freewheeling diodes (Rohm SCS120AG) are applied. This combination exhibits extremely low switching losses as shown in Fig. 18. Even though the conduction losses of SiC diodes are slightly higher compared to those of fast-recovery Si diodes, the improved switching behavior compensates for this drawback.

For reactive power compensation, polypropylene film/foil capacitors are used because of their low losses and high current carrying capability at high frequencies [25]. The thermal stress is distributed on multiple discrete capacitors.

The proposed control strategy was implemented into a rapid prototyping system. A field programmable gate array (FPGA) is used to generate the gate signals and to monitor the currents and voltages. This is important because the series-series-compensated topology is not open circuit safe. If there is a sudden drop of the load or if the resonant currents exceed a threshold value, this is detected by the FPGA and the system is shut down safely.

A. *Coupling Factor Measurement*

First, for validating the FEM simulation model, the coupling factor $k = M/\sqrt{L_1 L_2}$ was measured at different air gaps and lateral offsets. The simulation was performed using the commercial 3D-FEM tool JMAG. In Fig. 8, the measured and simulated coupling factors at different coil positions are shown. If the air gap is increased from 100 to 170 mm, the coupling factor is approximately reduced by a factor of 2, from 0.45 to 0.24. If there is an additional lateral offset of 100 mm, the coupling factor is further reduced to 0.19. There is an excellent accordance between the simulation model and the measurements with an average deviation at all measured positions of only 3.8% (refer to Fig. 8).

The measured and simulated self-inductances L_1 and L_2 are depicted in Figs. 9 and 10. In the relevant operating range up to a lateral offset of 100 mm, the primary self-inductance L_1

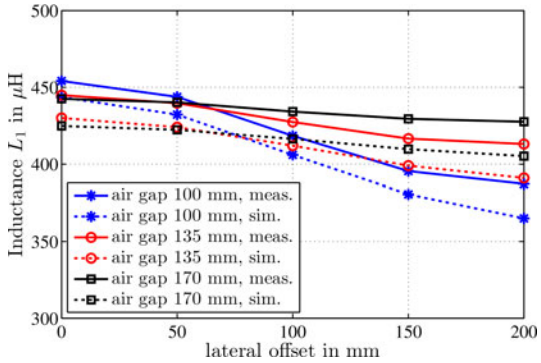

Fig. 9. Measured and simulated prim. inductance L_1 at different coil positions.

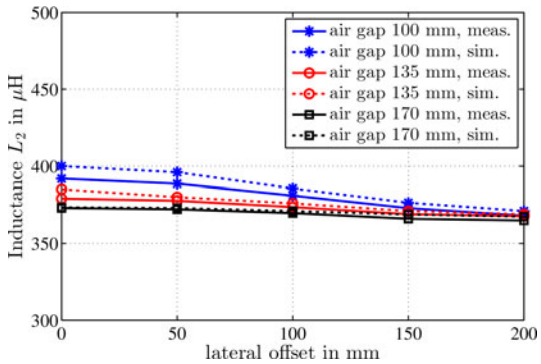

Fig. 10. Measured and simulated sec. inductance L_2 at different coil positions.

varies by 8% compared to its peak value of $L_1 = 454\,\mu H$ and the secondary self-inductance L_2 varies by 6% compared to its peak value of $L_2 = 392\,\mu H$. This variation causes a slight mistuning of the reactive power compensation. However, it is demonstrated experimentally that the impact on the operating point and efficiency is quite small, owing to the robustness of the proposed hard-switching topology. An adjustment of the operating frequency is not mandatory as it would be the case in most soft-switching topologies.

B. Voltage and Current Measurements

The primary and secondary voltage and current were measured in multiple operating points, using an oscilloscope. In Fig. 4, the voltage and current waveforms at nominal air gap (135 mm) and nominal output power (3 kW) are depicted. Accordingly, the voltage and current waveforms for an air gap of 100 mm (see Fig. 11) and 170 mm (see Fig. 12) are shown at the same output power of 3 kW.

The IPT system was designed for a minimal air gap of 100 mm. In this operating point, both the inverter and the rectifier are operating at their voltage limits (see Fig. 11). If the coupling factor further increases, the nominal power can no longer be transferred. The measured primary and secondary rms currents are $i_{1,\mathrm{rms}} = 8.5\,\mathrm{A}$ and $i_{2,\mathrm{rms}} = 8.3\,\mathrm{A}$, respectively.

In Fig. 12, it can be noted how the decreased coupling factor at 170 mm air gap affects the operating point of the dual-side controlled IPT system. As derived from the qualitative discussion (refer to Table I), both the primary and the secondary current are increased simultaneously to operate the IPT system in its optimal operating point: $i_{1,\mathrm{rms}} = 11.0\,\mathrm{A}$ and $i_{2,\mathrm{rms}} = 12.8\,\mathrm{A}$. Both the inverter and active rectifier are operated under hard-switching conditions with decreased pulse-widths α and β.

The partial load mode at 500 W output power and 135 mm air gap is depicted in Fig. 13. Both the primary and the secondary current are decreased by the dual-side control to $i_{1,\mathrm{rms}} = 3.5\,\mathrm{A}$ and $i_{2,\mathrm{rms}} = 4.7\,\mathrm{A}$. For comparison, the same partial load operating point was measured without operating the active rectifier (see Fig. 14). This corresponds to the conventional primary-side controlled series-series-compensated topology with passive

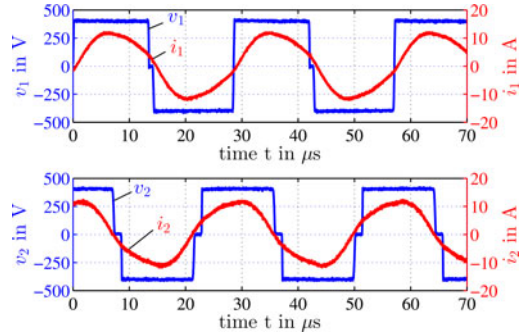

Fig. 11. Measured voltage and current waveforms at 100 mm air gap and 3 kW output power, $V_{1,\mathrm{DC}} = V_{2,\mathrm{DC}} = 400\,\mathrm{V}$.

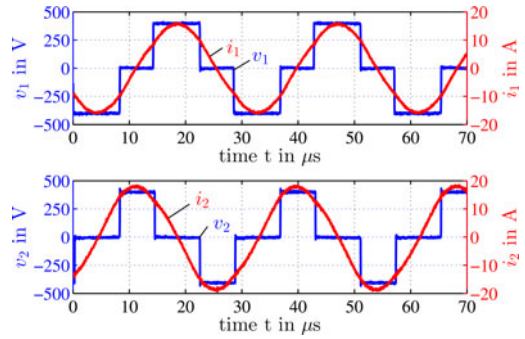

Fig. 12. Measured voltage and current waveforms at 170 mm air gap and 3 kW output power, $V_{1,\mathrm{DC}} = V_{2,\mathrm{DC}} = 400\,\mathrm{V}$.

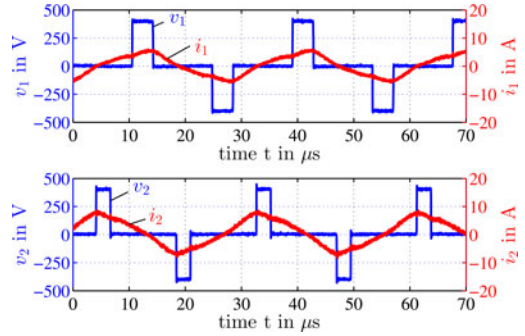

Fig. 13. Measured voltage and current waveforms at 135 mm air gap and 500 W output power (dual-side control), $V_{1,\mathrm{DC}} = V_{2,\mathrm{DC}} = 400\,\mathrm{V}$.

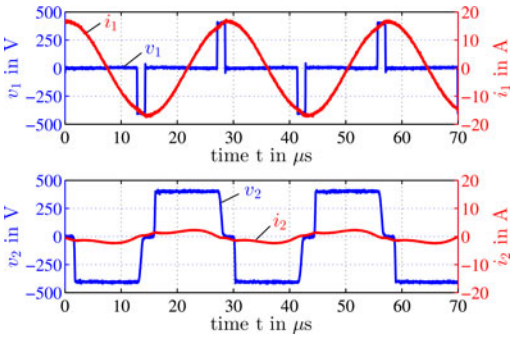

Fig. 14. Measured voltage and current waveforms at 135 mm air gap and 500 W output power (passive rectification), $V_{1,\mathrm{DC}} = V_{2,\mathrm{DC}} = 400\,\mathrm{V}$.

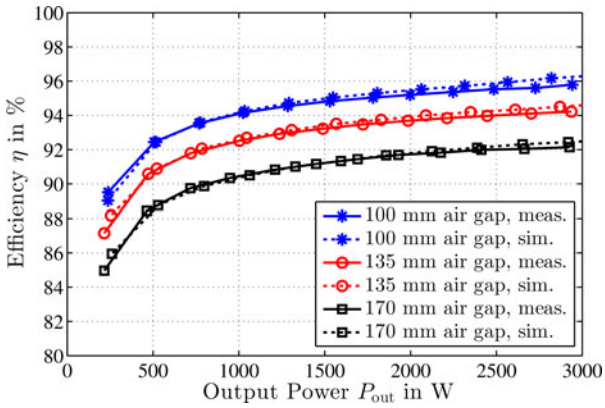

Fig. 15. Measured and simulated dc-to-dc efficiencies at different air gaps (no lateral offset, $V_{1,\mathrm{DC}} = V_{2,\mathrm{DC}} = 400\,\mathrm{V}$).

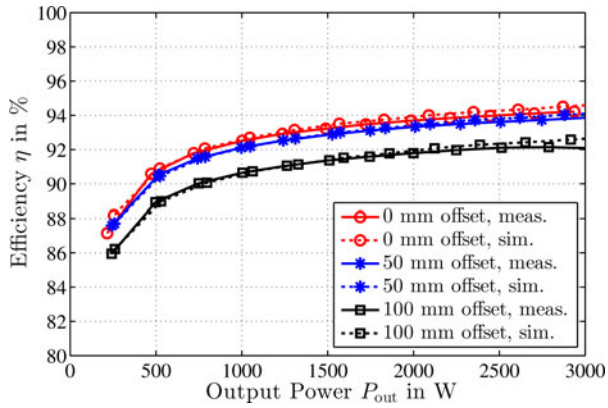

Fig. 16. Measured and simulated dc-to-dc efficiencies at different lateral offsets (135 mm air gap, $V_{1,\mathrm{DC}} = V_{2,\mathrm{DC}} = 400\,\mathrm{V}$).

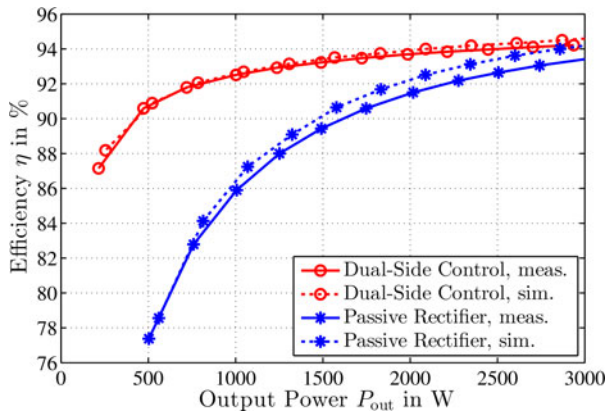

Fig. 17. Measured and simulated dc-to-dc efficiencies with passive rectification (135 mm air gap, $V_{1,\mathrm{DC}} = V_{2,\mathrm{DC}} = 400\,\mathrm{V}$).

rectification. As it was derived from the qualitative discussion (refer to Table I), also in partial load mode a constantly high current is circulating on the primary side: $i_{1,\mathrm{rms}} = 11.7\,\mathrm{A}$. The secondary current is reduced to $i_{2,\mathrm{rms}} = 1.5\,\mathrm{A}$. Especially, in this partial load operating point it is evident how the losses can be decreased with the dual-side control.

C. Efficiency Measurement

The total efficiency from dc to dc was measured at different operating points, using a power analyzer with a measurement error of less than 0.1%. It should be noted that the PFC front-end is not included in this measurement, so the total system efficiency from grid to battery would be somewhat smaller. The measurements were performed at a voltage level of $V_{1,\mathrm{DC}} = V_{2,\mathrm{DC}} = 400\,\mathrm{V}$ at three different air gaps and are compared to the simulation results in Fig. 15.

A peak efficiency of 95.8% at an air gap of 100 mm, a nominal efficiency of 94.2% at an air gap of 135 mm, and a minimal efficiency of 92.1% at an air gap of 170 mm are measured. Even at 500 W partial load, the measured efficiency does not drop below 88.4% at 170 mm air gap. Overall, the simulated efficiencies fit well to the measured values.

In Fig. 16, the measured and simulated efficiencies at different lateral offsets are shown at the nominal air gap of 135 mm. At a lateral displacement of 100 mm between the two coils, the efficiency drops from 94.2% to 92.1%. However, the nominal power of 3 kW can still be transferred. At higher lateral offsets, the efficiency drops significantly, and the power transfer has to be reduced.

Another measurement was performed without operating the MOSFETs of the active rectifier, to compare the dual-side power control with the primary-side power control with passive rectification (see Fig. 17). As expected, the efficiency in partial load mode drops significantly when using a passive rectifier, due to the high primary current. At an output power of 500 W, for instance, the measured efficiency drops to 77.4% compared to 90.6% with the dual-side control. Thus, in this operating point, the total losses can be reduced by more than a factor of 2.

D. Simulated Loss Distribution

The detailed simulated loss distribution and component-wise efficiencies at the nominal output power of 3 kW are depicted in Fig. 18. At the minimal air gap (100 mm), all losses are minimal. The inverter operates at its voltage limit, with the switching instants of the IGBTs close to the zero crossings of the primary current (see Fig. 11). Hence, the inverter switching losses are minimal. The same is true for the active rectifier, which

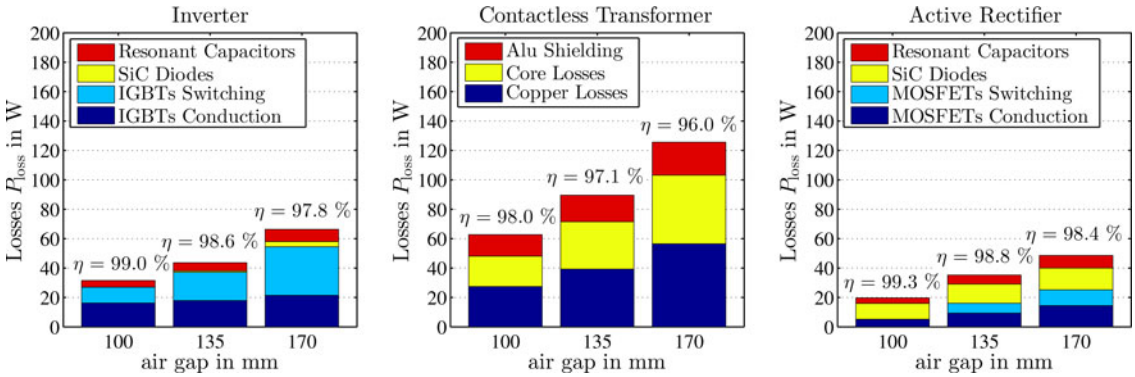

Fig. 18. Simulated loss distribution at different air gaps and 3 k W output power, $V_{1,\mathrm{DC}} = V_{2,\mathrm{DC}} = 400\,\mathrm{V}$.

is kept purely passive in this operating point. In the contactless transformer, the primary and secondary currents are minimal, causing 27 W copper losses, 21 W core losses, and 15 W eddy current losses in the aluminum shield.

At the maximum air gap of 170 mm, the primary and secondary currents have to be increased to achieve the same power transfer. This leads to increased losses in the contactless transformer: 56 W copper losses, 47 W core losses, and 22 W eddy current losses in the aluminum shield. In the inverter, not only the rms current is increased but also the switching instants of the IGBTs move farther away from the zero crossings of the primary current (refer to Fig. 12). Thus, a higher current has to be actively switched by the inverter IGBTs, causing switching losses of 33 W, compared to conduction losses of 21 W. In the active rectifier, the switching losses are as low as 11 W, compared to 14 W conduction losses of the two MOSFETs and 15 W conduction losses of the two SiC diodes. The losses in the resonant capacitors are 8.3 W on the primary side and 8.6 W on the secondary side.

Overall, the simulated component-wise efficiencies are in the range of 97.8% to 99.0% for the inverter, 96.0% to 98.0% for the contactless transformer, and 98.4% to 99.3% for the active rectifier, depending on the actual air gap. If the losses of the PFC rectifier are additionally considered, the total system efficiency at nominal output power, from grid to battery, is approximately in the range of 90% at 170 mm air gap to 94% at 100 mm air gap.

VI. Conclusion

A dual-side controlled, series-series-compensated topology and a corresponding control strategy were proposed to achieve high efficiencies over a wide operating range, even at low coupling factors and in partial load. An operating frequency of 35 kHz was found to be the optimal tradeoff to achieve a high efficiency of both the contactless transformer and the power electronic components. On a system level, the proposed topology does not require additional dc/dc converters on the infrastructure or vehicle side for power control and can thus be implemented with relatively low hardware effort.

A 3-kW hardware prototype was built, and the measurements are in excellent agreement with the simulation results. A peak efficiency of 95.8% at an air gap of 100 mm and a minimal efficiency of 92.1% at an air gap of 170 mm were measured, including all power electronic components except for the PFC rectifier. The partial load efficiency at 500 W output power and 135 mm air gap is still as high as 90.6%.

In contrast to the current trend to use soft-switching topologies and to increase the operating frequency, a hard-switching topology is preferred instead. With the further development of power semiconductors, especially wide-bandgap semiconductors, it can be expected that hard-switching topologies will gain even more importance in the future. The improved switching behavior of these devices would allow increasing the switching frequency of the proposed topology to 85kHz, which is currently under discussion as a future standard frequency for inductive vehicle chargers (SAE J2954). Beyond the application as a contactless vehicle charger, the dual-side controlled topology is a good candidate for all IPT applications where high efficiencies are required not only in the nominal operating point, but over a wide operating range, including partial load.

References

[1] G. A. Covic and J. T. Boys, "Inductive power transfer," *Proc. IEEE*, vol. 101, no. 6, pp. 1276–1289, Jun. 2013.
[2] E. Waffenschmidt and T. Staring, "Limitation of inductive power transfer for consumer applications," in *Proc. 13th Eur. Conf. Power Electron. Appl.*, 2009, pp. 1–10.
[3] D. J. Thrimawithana and U. K. Madawala, "A primary side controller for inductive power transfer systems," in *Proc. IEEE Int. Conf. Ind. Technol.*, 2010, pp. 661–666.
[4] U. K. Madawala and D. J. Thrimawithana, "New technique for inductive power transfer using a single controller," *IET Power Electron.*, vol. 5, no. 2, pp. 248–256, 2012.
[5] J. T. Boys, G. Covic, and A. W. Green, "Stability and control of inductively coupled power transfer systems," *IEE Proc. Electr. Power Appl.*, vol. 147, no. 1, pp. 37–43, 2000.
[6] C.-S. Wang, O. H. Stielau, and G. Covic, "Design considerations for a contactless electric vehicle battery charger," *IEEE Trans. Ind. Electron.*, vol. 52, no. 5, pp. 1308–1314, Oct. 2005.
[7] C.-Y. Huang, J. T. Boys, and G. A. Covic, "LCL pickup circulating current controller for inductive power transfer systems," *IEEE Trans. Power Electron.*, vol. 28, no. 4, pp. 2081–2093, Apr. 2013.
[8] H. H. Wu, A. Gilchrist, K. D. Sealy, and D. Bronson, "A high efficiency 5 kW inductive charger for EVs using dual side control," *IEEE Trans. Ind. Inform.*, vol. 8, no. 3, pp. 585–595, Aug. 2012.
[9] B. Schmuelling, S. G. Cimen, T. Vosshagen, and F. Turki, "Layout and operation of a non-contact charging system for electric vehicles," in *Proc. Power Electron. Motion Control Conf.*, 2012, pp. LS4d.4-1–LS4d.4-7.

[10] J. Huh, S. Lee, C. Park, G.-H. Cho, and C.-T. Rim, "High performance inductive power transfer system with narrow rail width for on-line electric vehicles," in *Energy Conver. Cong. Expo.*, 2010, pp. 647–651.
[11] C. Park, S.-W. Lee, and C.-T. Rim, "5m-off-long-distance inductive power transfer system using optimum shaped dipole coils," in *Proc. Power Electron. Motion Control Conf.*, 2012, vol. 2, pp. 1137–1142.
[12] J.-R. Sibue, G. Kwimang, J.-P. Ferrieux, G. Meunier, J. Roudet, and R. Periot, "A study of a contactless energy transfer system: Analytical design, virtual prototyping, and experimental validation," *IEEE Trans. Power Electron.*, vol. 28, no. 10, pp. 4690–4699, Oct. 2013.
[13] R. Bosshard, J. W. Kolar, J. Muehlethaler, I. Stevanovic, B. Wunsch, and F. Canales, "Modeling and η-α-pareto optimization of inductive power transfer coils for electric vehicles," *IEEE J. Emerg. Select. Topics Power Electron.*, vol. 3, no. 1, pp. 50–64, Mar. 2015.
[14] H. Cai, L. Shi, and Y. Li, "Harmonic-based phase-shifted control of inductively coupled power transfer," *IEEE Trans. Power Electron..*, vol. 29, no. 2, pp. 594–602, Feb. 2014.
[15] J. Tritschler, S. Reichert, and B. Goeldi, "A practical investigation of a high power, bidirectional charging system for electric vehicles," in *Proc. Eur. Conf. Power Electron. Appl.*, 2014, pp. 1–7.
[16] T. Diekhans, F. Stewing, G. Engelmann, H. van Hoek, and R. W. De Doncker, "A systematic comparison of hard- and soft-switching topologies for inductive power transfer systems," in *Proc. Elect. Drives Prod. Conf.*, 2014, pp. 1–8.
[17] J. Biela, D. Hassler, J. Miniböck, and J. W. Kolar, "Optimal design of a 5 kw/dm^3/98.3% efficient TCM resonant transition single-phase PFC rectifier," in *Proc. Power Electron. Conf.*, 2010, pp. 1709–1716.
[18] Y.-S. Kim, W.-Y. Sung, and B. Lee, "Comparative performance analysis of high density and efficiency PFC topologies," *IEEE Trans. Power Electron.*, vol. 29, no. 6, pp. 2666–2679, Jun. 2014.
[19] R. L. Steigerwald, "A comparison of half-bridge resonant converter topologies," *IEEE Trans. Power Electron.*, vol. 3, no. 2, pp. 174–182, Apr. 1988.
[20] M. Albach, J. Patz, H. Roßmanith, and A. Stadler, "Optimale wicklung = optimaler wirkungsgrad," *IEEE J. Elektronik Power*, pp. 38–45, 2010.
[21] H. Rossmanith, M. Doebroenti, M. Albach, and D. Exner, "Measurement and characterization of high frequency losses in nonideal litz wires," *IEEE Trans. Power Electron..*, vol. 26, no. 11, pp. 3386–3394, Nov. 2011.
[22] C. P. Steinmetz, "On the law of hysteresis," *Proc. IEEE*, vol. 72, no. 2, pp. 197–221, Feb. 1984.
[23] J. Reinert, A. Brockmeyer, and De Doncker, R. W., "Calculation of losses in ferro- and ferrimagnetic materials based on the modified Steinmetz equation," in *Proc. Ind. Appl. Conf.*, 1999, vol. 3, pp. 2087–2092.
[24] R. L. Stoll and P. Hammond, "Calculation of the magnetic field of rotating machines. Part 4: Approximate determination of the field and the losses associated with eddy currents in conducting surfaces," *Elect. Eng., Proc. Inst.*, 1965, vol. 112, no. 11, pp. 2083–2094.
[25] M. Brubaker, H. Kirbie, T. Hosking, and T. von Kampen, "System level considerations for integration of resonant capacitors in high power wireless charging," presented at the Conf. Elect. Roads Vehicles, Park City, Utah, USA, 2012.

Tobias Diekhans received the Diploma degree in electrical engineering from RWTH Aachen University, Aachen, Germany, in 2011.

He is currently working at the Corporate Research of Robert Bosch GmbH, Renningen, Germany. His research interests include the field of power electronics and inductive power transfer. His Ph.D. thesis is supervised by Prof. De Doncker.

Rik W. De Doncker (F'01) received the Ph.D. degree in electrical engineering from the Katholieke Universiteit Leuven, Leuven, Belgium, in 1986.

In 1987, he was appointed as a Visiting Associate Professor at the University of Wisconsin, Madison, WI, USA. After a short stay as an Adjunct Researcher with Interuniversity Microelectronics Centre, Leuven, he joined, in 1989, the Corporate Research and Development Center, General Electric Company, Schenectady, NY, USA. In 1994, he joined Silicon Power Corporation, a former division of General Electric Inc., as the Vice President of Technology. In 1996, he became a Professor at RWTH Aachen University, Aachen, Germany, where he currently leads the Institute for Power Electronics and Electrical Drives. Since 2006, he has been the Director of the E.ON Energy Research Center, RWTH Aachen University.

Dr. De Doncker was the President of the IEEE Power Electronics Society (PELS) in 2005 and 2006. He was the founding Chairman of the German IEEE Industry Applications Society PELS Joint Chapter. In 2002, he received the IEEE IAS Outstanding Achievement Award. In 2008, he received the IEEE PES Nari Hingorani Custom Power Award. In 2009, he led a VDE/ETG Task Force on Electric Vehicles. In 2010, he received an honorary doctor degree of TU Riga, Latvia. In 2013, he received the IEEE William E. Newell Power Electronics Award.